

# Origin of Two Distinct Peaks of Ice in the THz Region and Its Application for Natural Gas Hydrates Dissociation

Xuliang Zhu<sup>1</sup>, Jingwen Cao<sup>1</sup>, Xiaoling Qin<sup>1</sup>, Lu Jiang<sup>1</sup>, Yue Gu<sup>1</sup>, Haocheng Wang<sup>1</sup>, Yang Liu<sup>1</sup>,  
Alexander I. Kolesnikov<sup>2</sup>, Peng Zhang<sup>1\*</sup>

<sup>1</sup>School of Space Science and Physics, Shandong University, Weihai, 264209, China

<sup>2</sup>Neutron Scattering Division, Oak Ridge National Laboratory, Oak Ridge, Tennessee 37831,  
USA

## ABSTRACT

For liquid water in the far-infrared spectrum, the phonons of molecular vibrations constitute two bands with a narrow gap at around 30 meV. Interestingly, there are two distinct peaks for ice in this gap. We demonstrated that the two peaks come from two kinds of translational modes. Considering different O-O-O bending constants, we yielded two frequencies based on the ideal model of ice Ic. These two kinds of vibrational modes do not exist in liquid water due to the collapse of the rigid tetrahedral structure. Thus, a window remains for ice resonance absorption with minimum energy loss in liquid water. A new method to decompose gas hydrates was proposed by supplying two terahertz radiation energies at  $\sim 6.8$  and  $9.1$  THz. This is also applicable to flow assurance in the gas pipeline, aircraft deicer and so on. Experimental measurements are expected to verify this finding along with the rapid development of THz laser.

## 1. INTRODUCTION

As we deplete the readily accessible reserves, we will have to obtain natural gas from severe and remote conditions.<sup>1</sup> Despite the vast reserves of gas hydrates were found in the permafrost and deep oceans, the commercial exploitation is not yet realized so far concerning the economy and safety.<sup>2-5</sup>

In physics, the dissociation of gas hydrates is the process of inside hydrogen bonds (H-bonds) breaking. To supply energy to H-bonds of ice without absorption of surrounding water would be an efficient way. Interestingly, a window remains for ice in the far-infrared (IR) region. Fig.1 illustrates the absorption spectra of ice and liquid water recorded by inelastic neutron scattering (INS) experiments.<sup>6,7</sup> An energy gap from 200 to 300  $\text{cm}^{-1}$  is obvious for liquid water while there are two pronounced triangle peaks for ice Ih in this region. To clarify the difference, we should find out the origin of these two peaks.

For ice Ih, it is widely accepted that the peak seen at approximately 230  $\text{cm}^{-1}$  by IR absorption<sup>8</sup> and Raman scattering<sup>9</sup> is due to the molecular translational vibrations. In 1989, a high-resolution INS experiment first recognized two distinct peaks at 28.2 meV and 37.7 meV (i.e. 227  $\text{cm}^{-1}$  and 304  $\text{cm}^{-1}$  wavenumber) in the translational band.<sup>10</sup> This led to the question of where the strong peak comes from. Marchi et al. calculated the longitudinal optic–transverse optic mode splitting, which only yielded a gap of 10  $\text{cm}^{-1}$ .<sup>11,12</sup> Renker suggested two force constants along the optic axis and basal plane of ice Ih,<sup>13</sup> but this notion contradicted to the later report of polarized spectra of ice single crystals.<sup>10</sup> Li et al. further proposed a two-H-bond-strength model based on the electrostatic interactions of different hydrogen spatial configurations of adjacent molecules.<sup>14,15</sup> However, this model has not been widely accepted because of its large force constant ratio, which

1  
2  
3 has left a question unsolved until now.<sup>16-22</sup> Based on new clues from the study of ice Ic, we found  
4  
5 that the phonons in the translational band of ice are mainly composed of two kinds of vibrational  
6  
7 modes by computational simulations and analytic theory hereinafter.  
8  
9

## 10 11 **2. COMPUTATIONAL SETTINGS**

12  
13  
14 The first-principles density functional theory (DFT) calculations were conducted using the  
15  
16 CASTEP<sup>23</sup> program. The GGA functional was used in our simulations considering the noticeable  
17  
18 spatial variability of the electron density. We chose the RPBE<sup>24</sup> exchange-correlation (XC)  
19  
20 potential according to our test, which has acceptable accuracy for the intramolecular interaction.  
21  
22 To support the linear response method to calculate the phonon density of states (PDOS), we used  
23  
24 norm-conserving pseudopotentials. The self-consistent field tolerance (SCF) was set as  $1 \times$   
25  
26  $10^{-10}$  eV · atom<sup>-1</sup> for all ices.  
27  
28  
29  
30

31 The calculation of the 64-molecule ice Ih supercell was performed to mimic the hydrogen-  
32  
33 disordered structure. The energy cutoff for electronics states was set as 830.0 eV. The k-points  
34  
35 grid was  $3 \times 2 \times 2$ . The primitive cell of ice XI contains four molecules was calculated. The  
36  
37 energy cutoff was set as 750 eV. The k-points grid was  $6 \times 6 \times 3$ . The primitive cell of hydrogen-  
38  
39 ordered Ic contains two molecules was calculated. The energy cutoff was 1200 eV and the k-points  
40  
41 grid is  $7 \times 7 \times 8$ .  
42  
43  
44  
45

## 46 47 **3. RESULTS AND DISCUSSION**

### 48 49 **3.1. Simulation strategy**

50  
51  
52 Fig. 2 presents the Ih spectrum compared with three simulated ice phases. Two peaks are distinctly  
53  
54 seen in the experimental spectrum at 226 and 303 cm<sup>-1</sup>. We have investigated the hydrogen-ordered  
55  
56  
57  
58  
59  
60

1  
2  
3 model of ice Ic and found that there are only two kinds of molecular translational modes to  
4 constitute the two peaks.<sup>25</sup> The molecular configurations of any ice phase are subject to Bernal–  
5 Fowler ice rules.<sup>26</sup> Water molecules are oriented such that one molecule links four neighbors by  
6 H-bonds to form a tetrahedral geometry. We inserted a tetrahedron diagram in Fig. 2. Regarding  
7 the translational motion of a molecule, we regarded the oxygen as approximately the mass center.  
8 Considering the central molecule, there is a vibrational mode stretching along the HOH bisector  
9 (red line). To maintain a static mass center of a primitive cell, four neighbors vibrate in opposite  
10 direction. In other words, for one molecule, the four linked H-bonds oscillate simultaneously to  
11 yield a strong vibration; this is called the four-bond mode. Meanwhile, two vibrating directions  
12 exist perpendicular to the four-bond mode. This kind of vibration involves only two H-bonds,  
13 whereas the other two remain unchanged; this is called the two-bond mode and possesses a weaker  
14 frequency. The strengths ratio is  $\sqrt{2}$  according to simple harmonic oscillator model. For the  
15 dynamic processes, please see the supporting information (SI-1). Later, we also found this  
16 phenomenon in ice XIV, XVI, XVII, VIII, VII, II, and XV.<sup>27-32</sup> Herein, we explained the two peaks  
17 of the most common phase, ice Ih, by comparative analysis with ice XI.  
18  
19  
20  
21  
22  
23  
24  
25  
26  
27  
28  
29  
30  
31  
32  
33  
34  
35  
36

37  
38 Ice XI, the hydrogen-ordered counterpart of Ih, has four molecules in one primitive cell and  
39 therefore yield nine vibrational modes in the translational band.<sup>24</sup> The modes at 47, 52, and 168  
40  $\text{cm}^{-1}$  are the relative slip of neighboring layers along the y-, x-, and z-axes. As shown in Fig. 3, the  
41 modes at 310 and 308  $\text{cm}^{-1}$  are strong vibrations similar to the mode at 321  $\text{cm}^{-1}$  of Ic. The other  
42 four modes at 210, 220, 225, and 229  $\text{cm}^{-1}$  are non-degenerate two-bond modes similar to the mode  
43 at 230  $\text{cm}^{-1}$  of Ic. The average ratio of these two categories is also 1.4. Considering the distribution  
44 of these six modes, we fitted the spectrum curve, as shown in Fig. 4(a). The two main peaks of ice  
45 XI in Fig. 2 are obviously contributed by these two kinds of vibrational modes. Due to the  
46  
47  
48  
49  
50  
51  
52  
53  
54  
55  
56  
57  
58  
59  
60

consistency between XI and Ih, we reasonably regarded the two peaks of Ih as above two translational modes.

The calculation for ice Ih was performed with a 64-molecule supercell to mimic the hydrogen-disordered structure. The number of normal modes in the translation region is  $64 \times 3 - 3 = 189$ . We compiled a customized program to distinguish the mode type (please see the source code for details from the supporting information SI-2). Fig. 4(b) shows that the integrated distributions of the four-bond modes and two-bond modes can be clearly classified into two main peaks. Some values overlap because oxygen is assumed the molecular center of mass. The geometry of ice Ih is hexagonal ( $P6_3/mmc$ ), that of ice XI is orthorhombic ( $Cmc2_1$ ), and ice Ic has a cubic crystal structure ( $Fd\bar{3}m$ ). Because they all present two characteristic peaks, we deduced that the space group and hydrogen-ordered or disordered status have little influence on the molecule vibrational modes. The origin is from the local tetrahedral structure with 4-degree rotation–inversion symmetry.

### 3.2. Analytic theory

Take the hydrogen-ordered Ic as the ideal model. The primitive cell contains two molecules. Treat molecules as mass points O, thus the degree of freedom in one cell is 6. The lattice vectors are  $\mathbf{a}_1 = d\left(\sqrt{\frac{2}{3}}, \sqrt{\frac{2}{3}}, \frac{2}{\sqrt{3}}\right)$ ,  $\mathbf{a}_2 = d\left(\sqrt{\frac{2}{3}}, -\sqrt{\frac{2}{3}}, \frac{2}{\sqrt{3}}\right)$ ,  $\mathbf{a}_3 = d\left(\sqrt{\frac{2}{3}}, \sqrt{\frac{2}{3}}, -\frac{2}{\sqrt{3}}\right)$ , where  $d$  is the O-O bond length at equilibrium. The position vectors of two molecules are respectively at

$$\begin{cases} \mathbf{x}\left(\begin{smallmatrix} - \\ 0 \end{smallmatrix}\right) = \mathbf{0} + \mathbf{u}\left(\begin{smallmatrix} - \\ 0 \end{smallmatrix}\right) \\ \mathbf{x}\left(\begin{smallmatrix} - \\ 1 \end{smallmatrix}\right) = d\left(0, \sqrt{\frac{2}{3}}, \frac{1}{\sqrt{3}}\right) + \mathbf{u}\left(\begin{smallmatrix} - \\ 1 \end{smallmatrix}\right) \end{cases} \quad (1)$$

where  $\mathbf{u}\left(\begin{smallmatrix} - \\ k \end{smallmatrix}\right)$  is the small displacement from equilibrium. The position of molecules in a

complete lattice can be taken as

$$\mathbf{x}\left(\begin{smallmatrix} l_{ik} \\ k \end{smallmatrix}\right) = \mathbf{x}\left(\begin{smallmatrix} - \\ k \end{smallmatrix}\right) + \sum_{j=1}^3 l_{ik}^j \mathbf{a}_j, \quad (2)$$

where  $k$  is the base index which differs molecules in a cell,  $l_{ik}$  is the cell index. We only consider the forces between the adjacent four molecules, so we define  $l_{ik}$  as  $l_{00} = (0,0,0)$ ,  $l_{10} = (1,0,0)$ ,  $l_{20} = (1,0,1)$ ,  $l_{30} = (1,1,1)$ ;  $l_{01} = (0,0,0)$ ,  $l_{11} = (-1,0,0)$ ,  $l_{21} = (-1,0,-1)$ ,  $l_{31} = (-1,-1,-1)$ .

### 3.2.1. H-bond stretching energy

Each O-O bond-stretching energy (H-bond) is exactly equal in our approximation. The four bonds connected to molecule  $\mathbf{x}\left(\begin{smallmatrix} - \\ 0 \end{smallmatrix}\right)$  can be taken as vectors

$$\mathbf{d}_{i0} = \mathbf{x}\left(\begin{smallmatrix} l_{i1} \\ 1 \end{smallmatrix}\right) - \mathbf{x}\left(\begin{smallmatrix} - \\ 0 \end{smallmatrix}\right), \quad (3)$$

and the four bonds connected to molecule  $\mathbf{x}\left(\begin{smallmatrix} - \\ 1 \end{smallmatrix}\right)$  is

$$\mathbf{d}_{i1} = \mathbf{x}\left(\begin{smallmatrix} l_{i0} \\ 0 \end{smallmatrix}\right) - \mathbf{x}\left(\begin{smallmatrix} - \\ 1 \end{smallmatrix}\right). \quad (4)$$

The O-O bond-stretching energy

$$\Phi = \frac{1}{4} \kappa \sum_{k=0}^1 \sum_{i=0}^3 (|\mathbf{d}_{ik}| - d)^2, \quad (5)$$

where the factor 1/4 is to subtract the double-counted potential energy. We use index  $\alpha = 1, 2, \dots, 6$  for the generalized coordinates. Expand  $\Phi$  as far as a function of quadratic terms of molecule displacements  $\mathbf{u}\left(\begin{smallmatrix} l \\ k \end{smallmatrix}\right)$ ,

$$\Phi = 0 + \frac{1}{2} \sum_{\alpha, \beta=1}^6 \Phi_{\alpha\beta} \left(\begin{smallmatrix} l & l' \\ k & k' \end{smallmatrix}\right) u_{\alpha}\left(\begin{smallmatrix} l \\ k \end{smallmatrix}\right) u_{\beta}\left(\begin{smallmatrix} l' \\ k' \end{smallmatrix}\right) + \dots, \quad (6)$$

the coefficient

$$\Phi_{\alpha\beta} \begin{pmatrix} l & l' \\ k & k' \end{pmatrix} = \left( \frac{\partial^2 \Psi}{\partial u_{\alpha}^{(l)} \partial u_{\beta}^{(l')}} \right)_0 = \begin{pmatrix} \frac{4}{3}\kappa & 0 & 0 & -\frac{4}{3}\kappa & 0 & 0 \\ 0 & \frac{4}{3}\kappa & 0 & 0 & -\frac{4}{3}\kappa & 0 \\ 0 & 0 & \frac{4}{3}\kappa & 0 & 0 & -\frac{4}{3}\kappa \\ -\frac{4}{3}\kappa & 0 & 0 & \frac{4}{3}\kappa & 0 & 0 \\ 0 & -\frac{4}{3}\kappa & 0 & 0 & \frac{4}{3}\kappa & 0 \\ 0 & 0 & -\frac{4}{3}\kappa & 0 & 0 & \frac{4}{3}\kappa \end{pmatrix}.$$

(7)

### 3.2.2. O-O-O bond-bending energy

At the equilibrium, the O-O-O bond angles are all equal to  $\theta = \arccos\left(-\frac{1}{3}\right)$ . With displacements, the four O-O-O bond angles of the  $k^{\text{th}}$  molecule as the vertex are

$$\theta_{k,ij} = \arccos \frac{\mathbf{d}_{ik} \cdot \mathbf{d}_{jk}}{|\mathbf{d}_{ik}| |\mathbf{d}_{jk}|}, i \neq j. \quad (8)$$

The O-O-O bond-bending energy

$$\Psi = \frac{1}{2} \sum_{i=0}^2 \sum_{j=i+1}^3 [G_{0,ij}(\theta_{0,ij} - \theta)^2 + G_{1,ij}(\theta_{1,ij} - \theta)^2], \quad (9)$$

we assume the O-O-O bond-bending energies  $G$  are different, set  $\text{O}\cdots\text{H}-\text{O}-\text{H}\cdots\text{O}$  bond-bending force constant as  $G_a$ , that  $\text{O}-\text{H}\cdots\text{O}\cdots\text{H}-\text{O}$  as  $G_b$ , and that  $\text{O}-\text{H}\cdots\text{O}-\text{H}\cdots\text{O}$  as  $G_c$ .

It corresponds to  $G_a = G_{0,02} = G_{1,13}$ ,  $G_b = G_{0,13} = G_{1,02}$ ,  $G_c = G_{0,01} = G_{0,03} = G_{0,12} = G_{0,23} = G_{1,01} = G_{1,03} = G_{1,12} = G_{1,23}$ . Expand  $\Psi$ , the coefficients of expansion are as follows

$$\Psi_{\alpha} = \left( \frac{\partial \Psi}{\partial u_{\alpha}^{(l)}} \right)_0 = 0, \quad (10)$$

$$\Psi_{\alpha\beta} \begin{pmatrix} l & l' \\ k & k' \end{pmatrix} = \left( \frac{\partial^2 \Psi}{\partial u_{\alpha}^{(l)} \partial u_{\beta}^{(l')}} \right)_0 =$$

$$\begin{pmatrix}
 \frac{32G_c}{3d^2} & 0 & 0 & -\frac{32G_c}{3d^2} & 0 & 0 \\
 0 & \frac{32G_c}{3d^2} & 0 & 0 & -\frac{32G_c}{3d^2} & 0 \\
 0 & 0 & \frac{16(G_a + G_b)}{3d^2} & 0 & 0 & -\frac{16(G_a + G_b)}{3d^2} \\
 -\frac{32G_c}{3d^2} & 0 & 0 & \frac{32G_c}{3d^2} & 0 & 0 \\
 0 & -\frac{32G_c}{3d^2} & 0 & 0 & \frac{32G_c}{3d^2} & 0 \\
 0 & 0 & -\frac{16(G_a + G_b)}{3d^2} & 0 & 0 & \frac{16(G_a + G_b)}{3d^2}
 \end{pmatrix}. \quad (11)$$

### 3.2.3. Dynamic matrix

The Lagrangian of each cell is

$$L = \frac{1}{2}m\sum_{\alpha=1}^6 \dot{u}_{\alpha}^2 + \Phi + \Psi, \quad (12)$$

the dynamic matrix is

$$k_{\alpha\beta} = \Phi_{\alpha\beta} + \Psi_{\alpha\beta}. \quad (13)$$

Thus, we get three eigenvalues and the two weak ones among them are degenerate. The vibrational frequencies are proportional to the square roots of the eigenvalues of  $k_{\alpha\beta}$

$$\omega_1 = \sqrt{\frac{1}{m} \left( \frac{32(G_a + G_b)}{3d^2} + \frac{8\kappa}{3} \right)}, \quad (14)$$

$$\omega_2 = \omega_3 = \sqrt{\frac{1}{m} \left( \frac{64G_c}{3d^2} + \frac{8\kappa}{3} \right)}. \quad (15)$$

The H-bond force constant  $\kappa$  can be derived from the equation 3.16 in ref. 33

$$K = \frac{\kappa}{4\sqrt{3}d}. \quad (16)$$

Using the O-O distance  $d = 2.798 \text{ \AA}$ , and the bulk modulus  $K = 8.82882 \text{ GPa}$  according to the simulation of Ic, this equation gives the force constant  $\kappa = 1.068 \text{ eV} \cdot \text{\AA}^{-2}$ . This model gives two

1  
2  
3 eigenvalues of translational frequencies According to the simulated values,  $\omega_1 = 320.76 \text{ cm}^{-1}$ ,  
4  
5  $\omega_2 = \omega_3 = 229.96 \text{ cm}^{-1}$  in Ic, we get

$$\begin{cases} G_a + G_b = 2.912 \text{ eV} \cdot \text{rad}^{-2} \\ G_c = 0.240 \text{ eV} \cdot \text{rad}^{-2} \end{cases} \quad (17)$$

6  
7  
8  
9  
10  
11  
12  
13 Assuming one identical O-O-O bending energy, we can only get one eigenvalue from formula  
14  
15 (13). That is why the modeling by Bertie,<sup>34</sup> and Faure<sup>35</sup> et al. could not get the splitting frequencies  
16  
17 above 28 meV. Herein, we proved that there are two frequencies in the ideal model by mechanical  
18  
19 analysis.

#### 20 21 22 23 24 **4. CONCLUSIONS**

25  
26 We proved that the origin of two distinct peaks seen in many ices in the far-infrared region is from  
27  
28 two kinds of intrinsic translational modes. However, these two peaks may not that apparent in  
29  
30 high-pressure phases as shown from INS.<sup>15</sup> Our simulations show that the two intrinsic  
31  
32 translational modes is a general rule among ice family. Under high pressure, the distributions of  
33  
34 two kinds of modes may overlap due to structure deformations of the local tetrahedral geometry.  
35  
36 The only exception is ice X which no H-bonds exist in this structure under extreme pressure. Our  
37  
38 investigations show that two peaks may exist in clathrate ice, such as ice XVI and XVII.

39  
40  
41  
42  
43 The H-bonded structure of liquid water is a long-debating issue too. Whatever homogeneous<sup>36,37</sup>  
44  
45 view or heterogeneous<sup>38,39</sup> view on liquid water structure, no long-range ice structures exist.  
46  
47 Therefore, no above two modes too. Although the molecular rotation band presents a great redshift  
48  
49 compared with Ih, a narrow gap at around 30 meV is left. We have reported the similar two peak  
50  
51 positions of ice XVI and XVII,<sup>28,29</sup> the S-II and S-I types of gas hydrates respectively. Provided  
52  
53 two THz radiation energy (at ~6.8 and 9.1 THz) supplying to gas hydrates, the resonance  
54  
55  
56  
57  
58  
59  
60

1  
2  
3 absorptions may decompose the ice clathrate to release the guest molecules with minimum energy  
4 loss. Besides, antifreeze is used in the gas-pipeline flow assurance in the oil and gas industry.<sup>40</sup>  
5  
6  
7 When frozen contaminants on the aircraft, it interferes with the aerodynamic properties.<sup>41</sup> Since  
8  
9  
10 the THz laser could bypass certain obstacles, this technique is also useful for flow assurance in the  
11  
12 gas pipeline, aircraft deicer and so on. Difference-frequency generation (DFG) and THz-QCL are  
13  
14 candidate THz sources.<sup>42</sup> Hu and co-workers have reported the THz laser that can be tuned up to  
15  
16 7 THz at present.<sup>43</sup> With the rapid development of THz laser, a novel technique for energy recovery  
17  
18 from gas hydrates is expected.  
19  
20  
21

## 22 **ASSOCIATED CONTENT**

### 23 24 25 **Supporting Information**

26  
27  
28  
29 The following files are available free of charge.

30  
31 Dynamic process of two kinds of translational modes of water molecules (mp4);

32  
33 Source code of a self-compiled program to distinguish the mode type (PDF).  
34  
35

## 36 **AUTHOR INFORMATION**

### 37 38 39 **Corresponding author**

40  
41  
42 E-mail.: zhangpeng@sdu.edu.cn; Tel.: +86-631-568-8751  
43  
44

### 45 **ORCID**

46  
47 Peng Zhang: 0000-0002-1099-6310  
48  
49

### 50 **Notes**

51  
52  
53 The authors declare no competing financial interest.  
54  
55

### 56 **Acknowledgments**

57  
58  
59  
60

We appreciate ISIS at the Rutherford-Appleton Laboratory, UK, for access to neutron scattering facilities. The numerical calculations were done in the Supercomputing Center, Shandong University, Weihai. A.I.K. was supported by the Scientific User Facilities Division, Office of Basic Energy Sciences, US Department of Energy.

## References

- (1) Sloan, E. D. Fundamental principles and applications of natural gas hydrates. *Nature* **2003**, 426, 353-359.
- (2) Kim, H. C.; Bishnoi, P. R.; Heidemann, R. A.; Rizvi, S. S. H. Kinetics of methane hydrate decomposition. *Chem. Eng. Sci.* **1987**, 42, 1645-1653.
- (3) Li, X. S.; Wan, L. H.; Li, G.; Li, Q. P.; Chen, Z. Y.; Yan, K. F. Experimental investigation into the production behavior of methane hydrate in porous sediment with hot brine stimulation. *Ind. Eng. Chem. Res.* **2008**, 47, 9696-9702.
- (4) Li, G.; Li, X. S.; Tang, L. G.; Tang, Y.; Zhang, Y. Experimental investigation of production behavior of methane hydrate under ethylene glycol injection in unconsolidated sediment. *Energy Fuel* **2007**, 21, 3388-3393.
- (5) Hirohama, S.; Shimoyama, Y.; Wakabayashi, A.; Tatsuta, S.; Nishida, N. Conversion of CH<sub>4</sub>-Hydrate to CO<sub>2</sub>-Hydrate in Liquid CO<sub>2</sub>. *J. Chem. Eng. Japan* **1996**, 29, 1014-1020.
- (6) Wang, Y.; Dong, S. Neutron scattering studies of low-fraction H<sub>2</sub>O in silica gel. *Phys. Rev. B* **2003**, 68, 172201.

- 1  
2  
3 (7) Gaspar, A. M.; Marques, M. A.; Cabaco, M. I. de Barros Marques, M. I.; Kolesnikov, A.  
4 I.; Tomkinson, J; Li, J. C. Structure and dynamics of concentrated aqueous solutions of  
5 aluminium chloride, beryllium chloride and aluminium bromide: Raman, inelastic  
6 neutron scattering and x-ray diffraction results. *J Phys Condens Matter* **2004**, 16, 6343-  
7 6364.  
8  
9  
10  
11  
12  
13  
14  
15 (8) Bertie, J. E.; Labbe, H. J.; Whalley, E. Absorptivity of ice I in the range 4000-30 cm<sup>-1</sup>. *J.*  
16 *Chem. Phys.* **1969**, 50, 4501-4519.  
17  
18  
19  
20  
21 (9) Wong, P. T. T.; Whalley, E. Optical spectra of orientationally disordered crystals. VI. The  
22 Raman spectrum of the translational lattice vibrations of ice Ih. *J. Chem. Phys.* **1976**, 65,  
23 829-836.  
24  
25  
26  
27  
28 (10) Li, J. C.; Ross, D. K.; Howe, L.; Tomkinson, J. Inelastic incoherent neutron scattering  
29 spectra of single crystalline and polycrystalline ICE Ih. *Physica B* **1989**, 156/157, 376-379.  
30  
31  
32  
33  
34 (11) Marchi, M.; Tse, J. S.; Klein, M. L. Lattice vibrations and infrared absorption of ice Ih. *J.*  
35 *Chem. Phys.* **1986**, 85, 2414-2418.  
36  
37  
38  
39 (12) Klug, D. D.; Tse, J. S.; Whalley, E. The longitudinal-optic-transverse-optic mode splitting  
40 in ice Ih. *J. Chem. Phys.* **1991**, 95, 7011-7012.  
41  
42  
43  
44 (13) Renker, B. in *Physics and Chemistry of Ice* (eds whalley, E., Hones, S. J. & Gold, L. W.)  
45 82-89 (Univ. of Toronto Press, **1973**).  
46  
47  
48  
49 (14) Li, J. C.; Ross, D. K.; Evidence for two kinds of hydrogen bond in ice. *Nature* **1993**, 365,  
50 327-329.  
51  
52  
53  
54  
55  
56  
57  
58  
59  
60

- 1  
2  
3 (15) Li, J. C. Inelastic neutron scattering studies of hydrogen bonding in ices. *J. Chem. Phys.*  
4 **1996**, 105, 6733-6755. Li, J. C.; Kolesnikov, A. I. *J. Mol. Liq.* **2002**, 100, 1-39.  
5  
6  
7  
8  
9 (16) Tse, J. S.; Klug, D. D. Comments on “Further evidence for the existence of two kinds of  
10 H-bonds in ice Ih” by Li et al. *Phys. Lett. A* **1995**, 198, 464-466.  
11  
12  
13  
14 (17) Morrison, I.; Jenkins, S. First principles lattice dynamics studies of the vibrational spectra  
15 of ice. *Physica B* **1999**, 263/264, 442-444.  
16  
17  
18  
19 (18) Klotz, S.; Strässle, Th.; Salzmann, C. G.; Philippe, J.; Parker, S. F. Incoherent inelastic  
20 neutron scattering measurements on ice VII: Are there two kinds of hydrogen bonds in ice?  
21 *Europhys. Lett* **2005**, 72, 576-582.  
22  
23  
24  
25  
26  
27 (19) He, X.; Sode, O.; Xantheas, S. S.; Hirata, S. Second-order many-body perturbation study  
28 of ice Ih. *J. Chem. Phys.* **2012**, 137, 204505.  
29  
30  
31  
32 (20) Zhang, P.; Tian, L.; Zhang, Z. P.; Shao, G.; Li, J. C. Investigation of the hydrogen bonding  
33 in ice Ih by first-principles density function methods. *J. Chem. Phys.* **2012**, 137, 044504.  
34  
35  
36  
37  
38 (21) Zhang, P.; Han, S. H.; Yu, H.; Liu, Y. A calculating proof on hydrogen bonding in ordinary  
39 ice by the first-principles density functional theory. *RSC Adv.* **2013**, 3, 6646-6649.  
40  
41  
42  
43 (22) Zhang, P.; Wang, Z.; Lu, Y. B.; Ding Z. W. The normal mode of lattice vibrations of ice  
44 XI. *Sci. Rep.* **2016**, 6, 29273-29281.  
45  
46  
47  
48  
49 (23) Clark, S. J. ; Segallii, M. D.; Pickardii, C. J.; Hasnip, P. J.; Probert, M. I. J.; Refson, K.;  
50 Payne, M. C. First principles methods using CASTEP. *Z. Kristallogr* **2005**, 220, 567-570.  
51  
52  
53  
54  
55  
56  
57  
58  
59  
60

- 1  
2  
3 (24) Hammer, B.; Hansen, L. B.; Nørskov, J. K. Improved adsorption energetics within density-  
4 functional theory using revised Perdew-Burke-Ernzerhof functionals. *Phys. Rev. B* **1999**,  
5 59, 7413-7421.  
6  
7  
8  
9  
10  
11 (25) Yuan, Z. Y.; Zhang, P.; Yao, S. K.; Lu, Y. B.; Yang, H. Z.; Luo, H. W.; Zhao, Z. J.  
12 Computational assignments of lattice vibrations of ice Ic. *RSC Adv.* **2017**, 7, 36801-36806.  
13  
14  
15  
16 (26) Bernal, J. D.; Fowler, R. H. A theory of water and ionic solution, with particular reference  
17 to hydrogen and hydroxyl ions. *J. Chem. Phys.* **1933**, 1, 515-548.  
18  
19  
20  
21 (27) Zhang, K.; Zhang, P.; Wang, Z. R.; Zhu, X. L.; Lu, Y. B.; Guan, C. B.; Li, Y. DFT  
22 simulations of the vibrational spectrum and hydrogen bonds of ice XIV. *Molecules* **2018**,  
23 23, 1781.  
24  
25  
26  
27  
28  
29 (28) Wang, Z. R.; Zhu, X. L.; Jiang, L.; Zhang, K.; Luo, H. W.; Gu, Y.; Zhang, P. Investigations  
30 of the hydrogen bonds and vibrational spectrum of clathrate ice XVI. *Materials* **2019**, 12,  
31 246.  
32  
33  
34  
35  
36  
37 (29) Zhu, X. L.; Yuan, Z. Y.; Jiang, L.; Zhang, K.; Wang, Z. R.; Luo, H. W.; Gu, Y.; Cao, J.  
38 W.; Qin, X. L.; Zhang, P. Computational analysis of vibrational spectrum and hydrogen  
39 bonds of ice XVII. *New J. Phys.* **2019**, 21, 043054.  
40  
41  
42  
43  
44  
45 (30) Gu, Y.; Zhu, X. L.; Jiang, L.; Cao, J. W.; Qin, X. L.; Yao, S. K.; Zhang, P. Comparative  
46 analysis on hydrogen bonds in ice VII and VIII. *J. Phys. Chem. C* **2019**, 123, 14880-14883.  
47  
48  
49  
50 (31) Cao, J. W.; Chen, J. Y.; Qin, X. L.; Zhu, X. L.; Jiang, L.; Gu, Y.; Yu, X. H.; Zhang, P. DFT  
51 investigations of the vibrational spectra and translational modes of ice II, *Molecules*, **2019**,  
52 24, 3135.  
53  
54  
55  
56  
57  
58  
59  
60

- 1  
2  
3 (32) Qin, X. L.; Zhu, X. L.; Cao, J. W.; Jiang, L.; Gu, Y.; Wang, X. C.; Zhang, P. Computational  
4 analysis of exotic molecular and atomic vibrations in ice XV, *Molecules*, **2019**, 24, 3115.  
5  
6  
7  
8 (33) Petrenko, V. F.; Whitworth, R. W. in *Physics of ice*, 56 (Oxford Univ. Press, 1999).  
9  
10  
11 (34) Bertie, J. E.; Whalley, E. Optical spectra of orientationally disordered crystals. II. Infrared  
12 spectrum of ice Ih and ice Ic from 360 to 50 cm<sup>-1</sup>. *J. Chem. Phys.* **1967**, 46, 1271-1284.  
13  
14  
15  
16  
17 (35) Faure, P. A dynamic model of crystal lattice of ice. *J. de physique* **1969**, 30, 214-220.  
18  
19  
20 (36) Niskanen, J.; Fondell, M.; Sahle, C. J.; Eckert, S.; Jay, R. M.; Gilmore, K.; Pietzsch, A.;  
21 Dantz, M.; Lu, X.; McNally, D. E.; Schmitt, T.; da Cruz, V. V.; Kimberg, V.;  
22 Gel'mukhanov, F.; Föhlisch, A. Compatibility of quantitative X-ray spectroscopy with  
23 continuous distribution models of water at ambient conditions. *Proc Natl Acad Sci USA*  
24 **2019**, 116, 4058-4063.  
25  
26  
27  
28  
29  
30  
31  
32 (37) Sastry, S.; Debenedetti, P. G.; Sciortino, F.; Stanley, H. E. Singularity-free interpretation  
33 of the thermodynamics of supercooled water. *Phys. Rev. E* **1996**, 53, 6144-6154.  
34  
35  
36  
37  
38 (38) Palmer, J. C.; Martelli, F.; Liu, Y.; Car, R.; Panagiotopoulos A. Z.; Debenedetti P. G.  
39 Metastable liquid-liquid transition in a molecular model of water. *Nature* **2014**, 510, 385-  
40 388.  
41  
42  
43  
44  
45 (39) Lee, M. S.; Baletto, F.; Kanhere, D. G.; Scandolo S. Far-infrared absorption of water  
46 clusters by first-principles molecular dynamics. *J. Chem. Phys.* **2008**, 128, 214506.  
47  
48  
49  
50  
51 (40) Shin, K.; Udachin, K. A.; Moudrakovski, I. L.; Leek, D. M., Alavi, S.; Ratcliffe, C. I.;  
52 Ripmeester J. A. Methanol incorporation in clathrate hydrates and the implications for oil  
53  
54  
55  
56  
57  
58  
59  
60

1  
2  
3 and gas pipeline flow assurance and icy planetary bodies. *Proc Natl Acad Sci USA* **3013**,  
4 110 (21), 8437-8442.  
5  
6  
7

8  
9 (41) Parent, O.; Ilinca, A. Anti-icing and de-icing techniques for wind turbines: Critical review.  
10 *Cold Reg. Sci. Technol.* **2011**, 65, 88-96.  
11  
12

13  
14 (42) Tonouchi M. Cutting-edge terahertz technology. *Nat. Photonics* **2007**, 1, 97-105.  
15  
16

17 (43) Khalatpour, A.; Reno, J. L.; Hu, Q. Phase-locked photonic wire lasers by  $\pi$  coupling. *Nat.*  
18 *Photonics* **2019**, 13, 47-53.  
19  
20  
21  
22  
23  
24  
25  
26  
27  
28  
29  
30  
31  
32  
33  
34  
35  
36  
37  
38  
39  
40  
41  
42  
43  
44  
45  
46  
47  
48  
49  
50  
51  
52  
53  
54  
55  
56  
57  
58  
59  
60

## TOC graphic

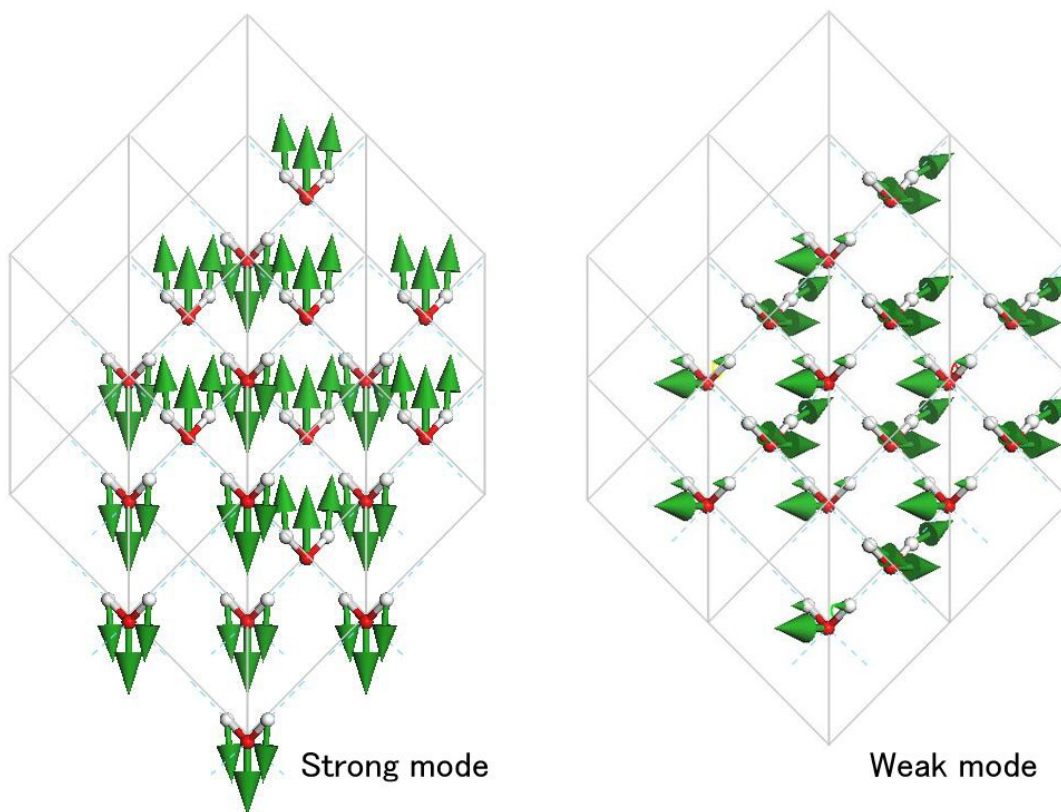


Diagram of the two basic hydrogen-bond vibrational modes in ideal ice Ic supercell.

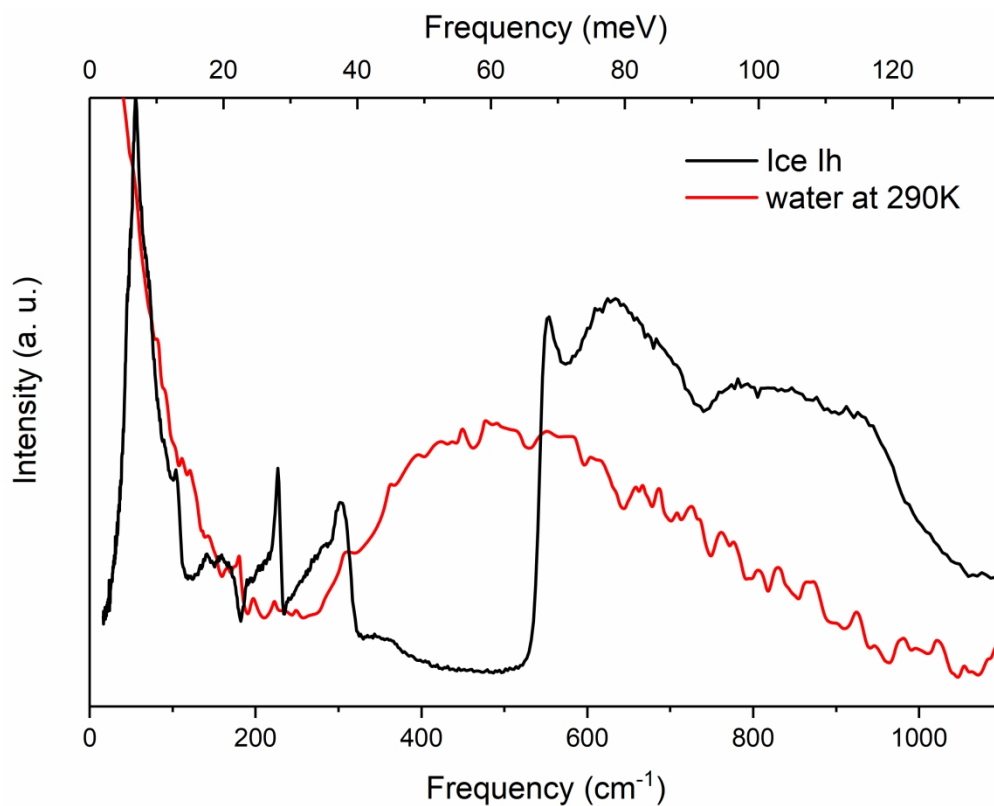


Figure 1. The absorption band of ice and liquid water in the far-IR region. Compared with the gap of liquid water at around 30 meV (from 200 to 310 cm<sup>-1</sup>), a window remains for energy absorption of ice.

246x197mm (300 x 300 DPI)

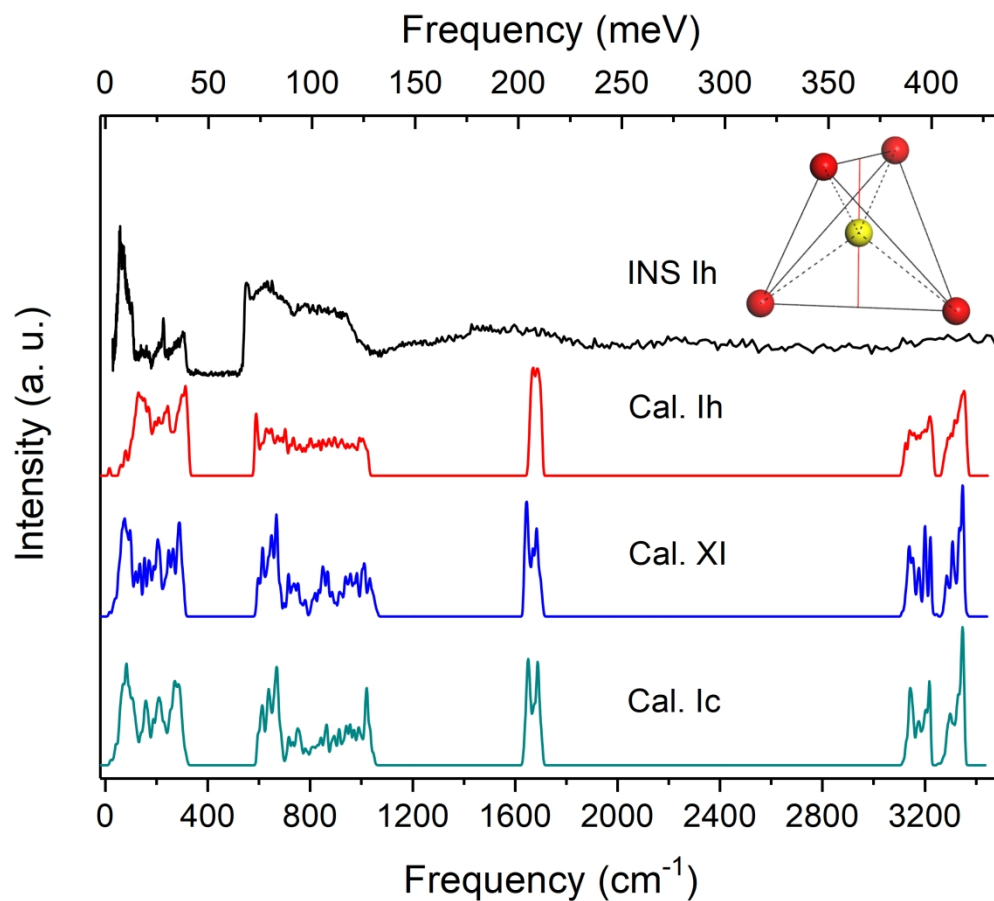


Figure 2. The vibrational spectra of ice Ih, XI, and Ic. The top curve is INS experimental data, and the others are calculated spectra. The two distinct H-bond peaks are almost identical. Insertion: diagram of the local tetrahedral structure.

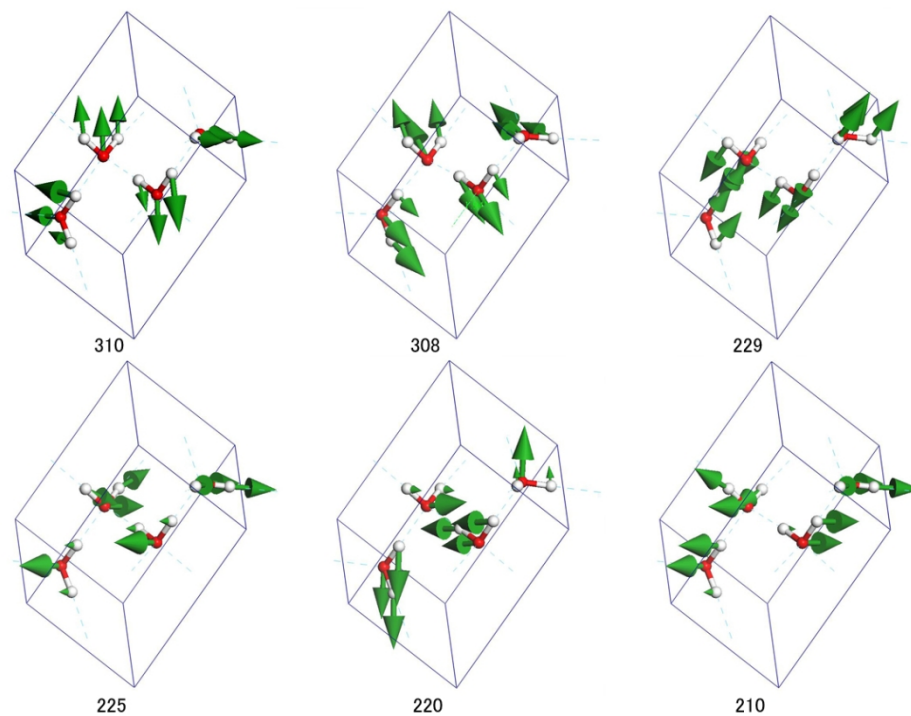


Figure 3. Six hydrogen-bond vibrational modes in ice XI. The number below each mode shows its frequency (cm<sup>-1</sup>). Modes of 310 and 308 are typical four-bond vibrations, and the others are two-bond vibrations.

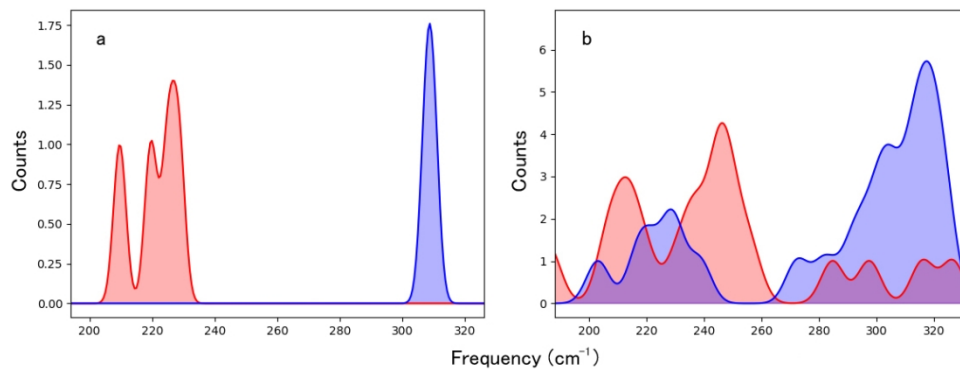


Figure 4. Distribution diagrams of four-bond modes (blue) and two-bond modes (red) of ice XI (a) and Ih (b). The classification standard of a stretch mode is judged by the vibrational direction of the molecule with the greatest amplitude in unit cell.